

Wavelet Spatio-Temporal Change Detection on multi-temporal SAR images

Rodney V. Fonseca, Rogério G. Negri, Aluísio Pinheiro, and Abdourrahmane Atto, *Senior Member, IEEE*

Abstract—We introduce WECS (Wavelet Energies Correlation Screening), an unsupervised procedure to detect spatio-temporal change points on multi-temporal SAR images. The procedure is based on wavelet approximation for the multi-temporal images, wavelet energy apportionment, and ultra-high dimensional correlation screening for the wavelet coefficients. We show WECS performance on simulated multi-temporal image data. We also evaluate the proposed method on a time series of 84 satellite images in a forest region at the border of Brazil and the French Guiana. The proposed method displays good results in covering change regions, with the additional benefit of having simple and fast computation.

Index Terms—Change detection, multi-temporal images, satellite images, wavelets.

I. INTRODUCTION

CHANGE detection is an important task performed in remote sensing image that allows researchers and engineers to identify and evaluate modifications on land surfaces captured by multi-temporal satellite images. Analyzing problems such as deforestation [1], rapid urbanization [2] and glacier melting [3], for example, are of great importance to study the dynamics of regions sensitive to climate changes and human activity. Furthermore, the increase on availability of satellite images in the past years raises the challenge of applying computationally cheap methods to images available at larger and larger from time to time. A review for change detection in multi-temporal remote sensing is given by [4].

Most methods used for change detection analysis can be classified either as supervised (training data is used to set up the method) or unsupervised (fully data-driven techniques). We shall focus in this work on unsupervised approaches, whose examples in the literature include the works of [5], [6], [7] and [8], for example. Many other proposals of methods vary in their motivations as well as in their applicability. Change detection in multi-temporal hyperspectral images is discussed in [9], [10], and [11]. [12] pursue change detection techniques via non-local means and principal component analysis. Compressed projection and image fusion are employed by [13]. Deep learning by slow feature analysis for change detection is the

This work was supported by FAPESP grants 2016/24469-6 and 2018/04654-9 and CNPq grants 309230/2017-9 and 310991/2020-0.

R. Fonseca and A. Pinheiro are with the Department of Statistics, University of Campinas, Campinas 13083-859, Brazil (e-mails: ra192588@dac.unicamp.br; pinheiro@ime.unicamp.br).

A. Atto is with the LISTIC - Polytech Annecy-Chambéry, Université de Savoie, 74944 Annecy le Vieux Cedex, France (e-mail: Abdourrahmane.Atto@univ-savoie.fr).

R. G. Negri is with the Department of Environmental Engineering, São Paulo State University, São José dos Campos, Brazil (e-mail: rogerio.negri@unesp.br).

subject of [14]. [15] proposes a change detection method driven by adaptive parameter estimation.

In this paper we analyze Synthetic Aperture Radar (SAR) images through an unsupervised wavelet method. Known to be not affected by weather, cloud and sunlight conditions, SAR images have been an important source of data for change detection methods in the literature [16]. Unsupervised analysis of such images consists in the steps of data denoising, pixel-level processing and change examination. Our idea is to explore the denoising property of wavelet transforms and apply a feature screening idea to identify change regions at pixels represented by wavelet coefficients. Wavelet methods present many advantages for a plethora of statistical applications [17] not only in remote sensing problems thanks to wavelet capabilities in capturing multiscale/multiresolution information. Their computational efficiency and sparseness are specially relevant for large images and other high-dimensional data [18]. Analysis of SAR images have been investigated under different approaches using wavelet methods, such as [19], [20], [21], [22]. However, the application of feature screening on wavelet coefficients is still a novel idea in change detection literature, and we show it has an interesting potential to provide good results even with simple algorithms.

We propose here a novel method for unsupervised spatio-temporal change detection in a time series of SAR images. Wavelet Energies Correlation Screening (WECS) is based upon correlation screening for energy apportionment on wavelet approximations. The spatial character of the change detection is attained on pixel level, whereas total energy measures for each image in the time series quantify changes happening across time. The idea behind WECS is built on ultra-high dimensional feature screening for the wavelet coefficients [23]. Such method is usually employed in high-dimensional regression models to reduce the problem's dimension by subsetting the available covariates in such a way that true covariates are among the chosen ones with high probability [24]. We show that by applying the feature screening idea on multi-temporal images, we obtain a fast and accurate method to cover change regions with good detection rates.

The rest of the text goes as follows. Section II introduces the problem and presents the proposed method. We show WECS performance on simulated multi-temporal image data in Section ???. In Section ?? we apply the proposed method to a time series of 85 satellite images in the border region of Brazil and the French Guiana, for images captured from November 08, 2015 to December 09 2017. Section IV concludes the paper with a discussion.

II. METHODOLOGY

Let $\mathcal{I}^{(1)}, \dots, \mathcal{I}^{(n)}$ be a set of matrices representing the images of some region of interest and n instants in time. These images may be relative to one SAR channel or a combination of channels; this will be specified when appropriate. Our goal is twofold: to find possible points in time where some relevant changes might have taken place at the region represented in $\mathcal{I}^{(m)}$, $m = 1, \dots, n$, and to find which regions are closely associated to the observed changes along time. We shall address these tasks by analyzing the bidimensional stationary discrete wavelet decomposition of $\mathcal{I}^{(m)}$. Stationary wavelets (also known as non-decimated or redundant wavelets) is a traditional de-noising method that can be efficiently applied to two-dimensional signals such as images [19], [25], [26]. After application of this wavelet transform to $\mathcal{I}^{(m)}$ at some appropriate resolution level $J \geq 1$, one of its by-products is a matrix of so called approximation wavelet coefficients $\mathbf{X}^{(m)}$, a smooth version of $\mathcal{I}^{(m)}$ with the same dimension. The higher $J \in \{1, \dots, \log_2(k)\}$ is, the smoother $\mathbf{X}^{(m)}$ gets, where k is the minimum between the numbers of rows and columns of $\mathcal{I}^{(m)}$. Many other aspects can be involved in wavelet analysis of images (e.g., different types of wavelet transform, choice of wavelet basis, thresholding of detail coefficients, etc.), but in the current work we focus on $\mathbf{X}^{(m)}$, which provides a simple way of performing wavelet smoothing and that gives interesting results; extensions based on further aspects of wavelet transforms are straightforward.

We can then consider further apportioning the total \mathbb{L}_2 energy of $\{\mathbf{X}^{(m)}\}$ as

$$\sum_{m=1}^n \|\mathbf{X}^{(m)}\|^2 = n\|\bar{\mathcal{I}}\|^2 + 2n\langle \bar{\mathbf{X}} - \bar{\mathcal{I}}, \bar{\mathcal{I}} \rangle + \sum_{m=1}^n \|\mathbf{X}^{(m)} - \bar{\mathcal{I}}\|^2, \quad (1)$$

where $\bar{\mathcal{I}} = n^{-1} \sum_{m=1}^n \mathcal{I}^{(m)}$, $\bar{\mathbf{X}} = n^{-1} \sum_{m=1}^n \mathbf{X}^{(m)}$ and $\|\mathbf{A}\|^2 = \sum_{i=1}^n \sum_{j=1}^m a_{ij}^2$ for a $n \times m$ matrix $\mathbf{A} = [a_{ij}]$. The last term in (1) measures deviations in time of $\mathbf{X}^{(m)}$ compared to an *average image* $\bar{\mathcal{I}}$, what motivates us to such deviations to detect change points in time. Since each element (pixel) in $\mathbf{X}^{(m)}$ also has a corresponding sequence of deviations in time, the relation of each local deviation to the overall measure can also be quantified, what allows us to detect changes in space. Such relation shall be computed in the present work with the Pearson correlation, what shares connections with the idea of feature screening employed in high-dimensional regression, as explained further. Other measures of change in time could be evaluated as well, such as squared differences of consecutive times $\|\mathbf{X}^{(m)} - \mathbf{X}^{(m-1)}\|^2$, $d(\mathbf{X}^{(m)}, \bar{\mathbf{X}})$ with $d(\cdot, \cdot)$ denoting some distance measure (e.g., Hellinger, Kullback-Leibler, etc.), among many other possibilities.

Let $X_{k,l}^{(m)}$ and $\bar{I}_{k,l}$ be the entry (k, l) of $\mathbf{X}^{(m)}$ and $\bar{\mathcal{I}}$, respectively. Computing $D_{k,l}^{(m)} = (X_{k,l}^{(m)} - \bar{I}_{k,l})^2$, we denote the matrix of squared mean differences as $\mathbf{D}^{(m)} = [D_{k,l}^{(m)}]$. We then analyze the time series given by

$$\mathbf{d}(m) = \sum_{k,l} D_{k,l}^{(m)} = \sum_{k,l} (X_{k,l}^{(m)} - \bar{\mathcal{I}}_{k,l})^2, \quad (2)$$

$m = 1, \dots, n$, which measure the temporal overall variation with respect to $\bar{\mathcal{I}}$.

The time points with highest values of $\mathbf{d}(m)$ represent the images for which the most expressive changes take place, where changes here are measured through \mathbb{L}_2 energy. Define the $n \times p$ matrix

$$\mathbf{D} = \begin{pmatrix} \text{vec}(\mathbf{D}(1))^T \\ \vdots \\ \text{vec}(\mathbf{D}(n))^T \end{pmatrix},$$

where $\text{vec}(\mathbf{D}^{(m)})$ is the $p \times 1$ vector of wavelet coefficients for time m and $p = \#\{k, l\}$ is total number of locations represented by $\mathbf{X}^{(m)}$, $m = 1, \dots, n$. Sparsity [27] on wavelet coefficients plays a special role here. We suppose a handful of coefficients drive the changes given by \mathbf{d} , so that the effective dimension of \mathbf{D} (number of locations where relevant changes occur), say s_d , is such that $s_d \ll p$. This can be represented as the following linear model

$$\mathbf{d} = \mathbf{D}\boldsymbol{\beta} + \boldsymbol{\xi} \quad (3)$$

where β is sparse, i.e., it has $p - s_d$ null elements, and $\xi^{(d)}$ is some $n \times 1$ random vector of errors.

In order to identify spatio-temporal changes, we employ the idea of ultra-high dimensional correlation screening [23] as follows. For each local squared mean deviation time series, given by individual elements of $\mathbf{D}^{(m)}$ across $m = 1, \dots, n$, consider the absolute value of its Pearson correlation with the overall squared mean deviations, given by \mathbf{d} :

$$R_{k,l} = |\text{corr } (\mathbf{D}_{k,l}, \mathbf{d})|,$$

where $\mathbf{D}_{k,l} = (D_{k,l}(1), \dots, D_{k,l}(n))^T$ is the time series of squared mean deviations of wavelet coefficients for the two-dimensional index $\{k, l\}$.

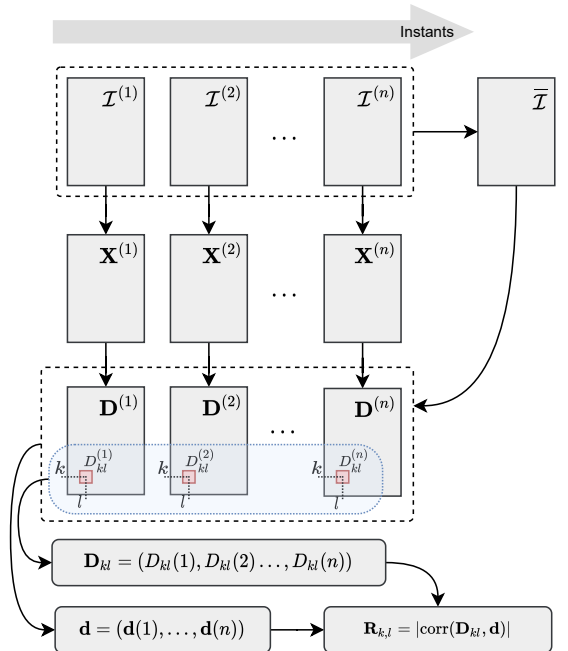


Fig. 1. Diagram of steps performed on WECS to compute an absolute correlation of a single point.

We have a matrix $\mathbf{R} = [R_{k,l}]$ of correlations of ultra-high dimension. Define the set of *important* indices for changes in images with respect to \mathcal{I} as $\mathcal{M}^* = \{(k,l) : \text{changes in } \{\mathcal{I}^{(m)}\}_{m=1}^n \text{ with respect to } \mathcal{I} \text{ are affected by changes in location corresponding to index } (k,l) \text{ in such images}\}$. This set coincides with the non-zero vectorized one-dimensional indices for the sparse representation of β in (3). We build the empirical set of indices flagged as corresponding to change locations by

$$\mathcal{M}_\tau = \{(k,l) : |R_{k,l}| > \tau\}, \quad (4)$$

where $\tau_d > 0$ is a convenient threshold value, function of n and J . Under some regularity conditions, the probability that \mathcal{M}_τ contains its target set satisfies

$$P(\mathcal{M}_\tau \supset \mathcal{M}^*) \rightarrow 1,$$

as $n \rightarrow \infty$ [23], where P denotes a probability measure. In other words, the empirical set \mathcal{M}_τ has high probability of detecting the correct change locations in \mathcal{M}^* when the number of observations n is large.

Further geometrical motivation for our proposal is given as follows. As defined by (2), we expect \mathbf{d} to be a vector with some few high values, say s_d , and $n - s_d$ smaller values. This segregates the multi-temporal images, since the former time points identify the images in which significant changes occur, while the latter indices identify time points with no major changes. Consider $U > L > 0$ such that the s_d highest values of \mathbf{d} are larger than U , and the $n - s_d$ smallest values of \mathbf{d} are smaller than L . We also take $\delta = U - L$. The indices defined by (4) are such that

$$\frac{\langle \mathbf{D}_{k,l}, \mathbf{d} \rangle}{\|\mathbf{D}_{k,l}\|_2 \|\mathbf{d}\|_2} > \tau,$$

i.e., such that $\sum_{m=1}^n D_{k,l}^{(m)} \mathbf{d}(m) > \tau \|\mathbf{D}_{k,l}\|_2 \|\mathbf{d}\|_2$. This can be rewritten as

$$\left| \sum_{m:\mathbf{d}(m)>U} D_{k,l}^{(m)} \right| - \left| \sum_{m:\mathbf{d}(m) < L} D_{k,l}^{(m)} \right| > \Delta,$$

for some arbitrary $\Delta \gg 0$ (which can be a function of n and J). Thence, when we employ correlation screening we select the two-dimensional wavelet indices which have the closest empirical directions to the vector of image temporal changes. Thus we are performing a truly spatio-temporal change detection in a single procedure.

III. EXPERIMENTS

In this section we shall evaluate the performance of WECS on two types of data sets. Initially, we generate simulated data where the level of noise and true change regions are known. For these images, we analyze different aspects of concerning the application of WECS and compare its performance with a standard change detection method. In the following application, real satellite data is employed, where the performance of WECS is evaluated on predefined change regions.

A. Simulated data analysis

In this section we apply the change detection methods above on simulated data of multi-temporal images. The simulated multi-temporal images ($n = 80$) is obtained by repeating a sequence of four images with different types of changes plus a noise. Examples of the first four of these images are shown in Figure 2. These images are generated from the sum of two matrices: a signal matrix with ones on entries where ellipses occur and zero elsewhere, and a noise matrix with random variables following a standard Gaussian distribution. The first image, $\mathcal{I}^{(1)}$, presents three elongated ellipses. The second image $\mathcal{I}^{(2)}$ has shorter and larger ellipses added. Smaller ellipses are then added to form $\mathcal{I}^{(3)}$ and $\mathcal{I}^{(4)}$. All the changes made that occur among subsequent images can be seen in Figure 3(a), which displays a matrix of zeros and ones that correspond, respectively, to locations without and with changes along time. Applying WECS to these images, we obtain a matrix \mathbf{R} of correlations between deviations of each \mathcal{I} entry with the total squared mean deviation. An example of \mathbf{R} is presented in Figure 3(b). For some choice of threshold τ on absolute values of \mathbf{R} , we obtain a matrix of zeros and ones that can be compared with the total true changes displayed in Figure 3(a).

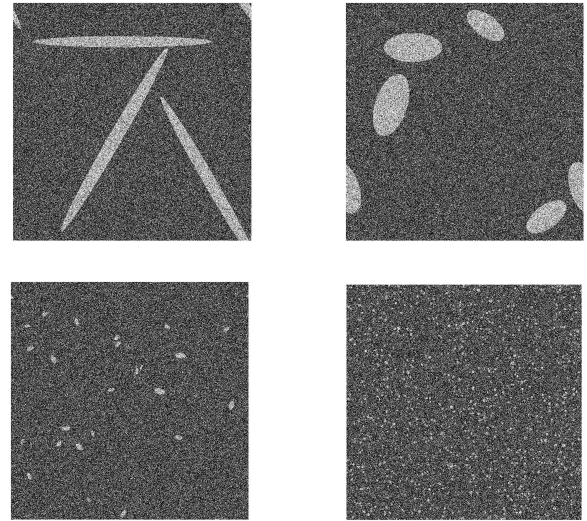


Fig. 2. Example of the first four simulated multi-temporal images. Features and changes come as white ellipses and dots.

Figure 3 illustrates a comparison of different approaches to detect accumulated changes. Panel (b) shows the result of WECS using Daubechies wavelet with two null moments (db2) and $J = 2$. Panel (c) presents the result of using aggregated absolute differences, a standard approach where the accumulation of changes are measured by a matrix $\mathbf{S} = \{\mathbf{S}_{k,l}\}$ with $S_{kl} = \sum_{m=2}^n |\mathcal{I}_{k,l}^{(m)} - \mathcal{I}_{k,l}^{(m-1)}|$. Finally, in Panel (d) we can see the result if $\mathbf{d}(m)$ is performed purely on the spatial domain, using $\mathcal{I}^{(m)}$ instead of $\mathbf{X}^{(m)}$ in the WECS formulation.

We compute ROC curves to compare the detection performance of different methods and to verify the influence of some tuning parameters of wavelet smoothing: the resolution level J and the choice of wavelet basis. Each detection method

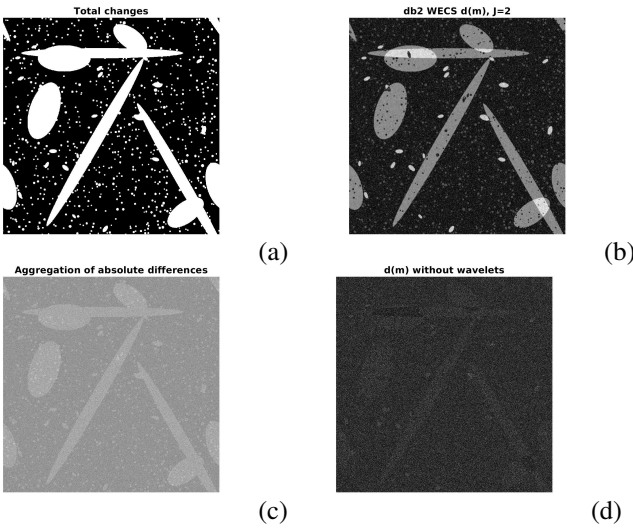


Fig. 3. Simulated images with changing ellipses. (a) Image composed by the total changes over time. (b) Proposed db2 WECS $\mathbf{d}(m)$ with $J = 2$; (c) Standard approach. (d) $\mathbf{d}(m)$ without wavelets.

generates a matrix of change detection measures (correlations in the case of WECS). The ROC curves present the performance of change detection by applying a threshold on these measures, in the following way:

- 1) Let R be the matrix of change measures. Compute the range $[r_{\min}, r_{\max}]$ of the values in R ;
- 2) Let $(r_{(1)}, \dots, r_{(100)})$ be equally space values between r_{\min} and r_{\max} ;
- 3) For each $k = 1, \dots, n$, check how many entries are there such that $R_{i,j} > r_{(k)}$ coincide with the element (i, j) where a change really occurs on the image of total changes. Dividing this number by the total number of changes gives the true positive rate.
- 4) For each $k = 1, \dots, n$, check how many entries are there such that $R_{i,j} > r_{(k)}$ do not coincide with the element (i, j) where a change really occurs. Dividing this number by the total number of entries where changes do not occur gives the false positive rate.
- 5) The ROC curve is the plot of true and false positive rates corresponding to each k .

Figure 4 presents the different ROC curves for change detection methods applied to the simulated data as follows. The effects of wavelet bases, level of decomposition, deep-learning feature extraction are shown on the ROC curves. We employ the following wavelet bases: Haar; Daubechies db2; Daubechies db4; Coiflets coif4; Symlets sym2 ; and Symlets sym4. Panel (c) presents the ROC curves for the proposed method under the aforementioned bases. On all instances $J = 2$ is employed. Comparing the ROC curves of all options, we can notice that Daubechies db2 and Symlets sym2 are the best choices. Panel (b) presents the ROC curves for five different levels of decomposition $J = \{1, 2, 3, 4, 5\}$ under the Daubechies db2 basis. Levels $J = 2, 3$ have a clear better performance, with a slight advantage to $J = 2$, since it is uses less levels on the decomposition. The overall performance of $J = 2$ warrants its use for the rest of the comparisons. Panel (d) shows

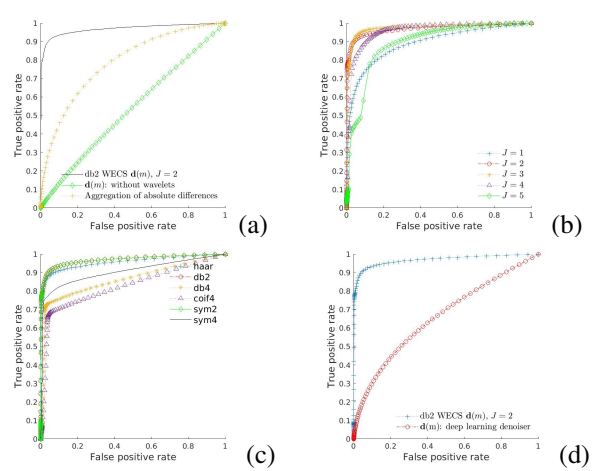


Fig. 4. ROC curves for detection of changing ellipses in simulated images and different methods. (a) The proposed methods in black (db2 WECS $\mathbf{d}(m)$) vs two non-wavelet methods: standard log-ratio aggregation (red stars); and $\mathbf{d}(m)$ (blue). (b) db2 $\mathbf{d}(m)$ with different levels. (c) $\mathbf{d}(m)$ with different wavelet bases and $J=2$; (d) The proposed db2 WECS $\mathbf{d}(m)$ (red circles) and $\mathbf{d}(m)$ with deep-learning feature extraction and without wavelets (yellow line).

how the proposed method performs in comparison to a deep learning feature extraction from a residual learning network [28]. WECS is applied with db2 wavelets and $J = 2$, whereas the other method applies WECS's idea, the only difference being that $\mathbf{X}^{(m)}$ is replaced by another smooth version of $\mathcal{I}^{(m)}$ that employs neural-networks trained to compete with wavelet smoothing. We can see that the ROC curves for images treated with a deep-learning method has a performance worse than that obtained with WECS. We finally have in Panel (a) the proposed WECS with db2 wavelets and $J = 2$ compared to two other non-wavelet methods. The first involves computing $\mathbf{d}(m)$ without wavelet smoothing, i.e., the squared deviations are computed using $\{\mathcal{I}^{(m)}\}$ instead of $\{\mathbf{X}^{(m)}\}$, and the classic method of analyzing aggregated absolute differences of $\{\mathcal{I}^{(m)}\}$. The ROC curves in Panel (a) show that the proposed WECS outperforms both the other two methods.

B. Actual remote sensing application

We employed the proposed change detection method on a series of 84 multi-date satellite images. The images were taken on a forest region at the border of Brazil and the French Guiana from 2015-12-26 to 2017-12-3. Each image has two channels (VV and VH) and 1538 by 1556 pixels. We perform a change detection wavelet analyses on the combined image by considering each observed entry as $\mathcal{I}_{k,l}^{(m)} = ((\text{VV}_{k,l}^{(m)})^2 + (\text{VH}_{k,l}^{(m)})^2)^{1/2}$, where VV and VH represent the matrices of observations from VV and VH channels, respectively.

A multi-resolution analysis based on a Symlet basis with filter of length 16 (symlet 8) is built. In order to have dimensions as power of 2, the matrices $\mathcal{I}_{k,l}$ are extended to a 2048×2048 matrix with $\mathcal{I}_{k,l}$ at the center and the remaining parts being completed with mirrored values at the borders. The wavelet transform at resolution level $J = 2$ is applied to these matrices and only the portion corresponding to the 1538×1556

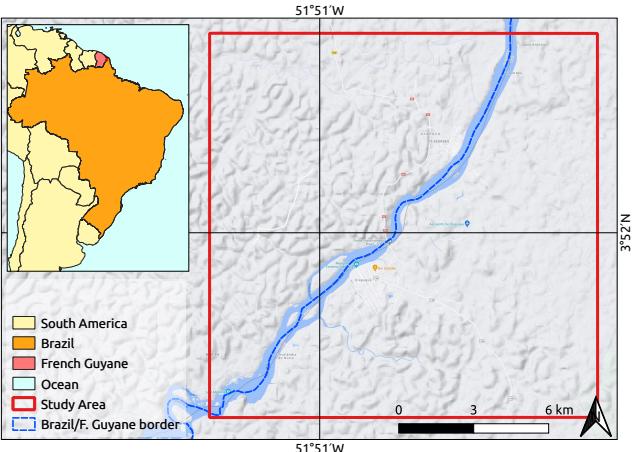
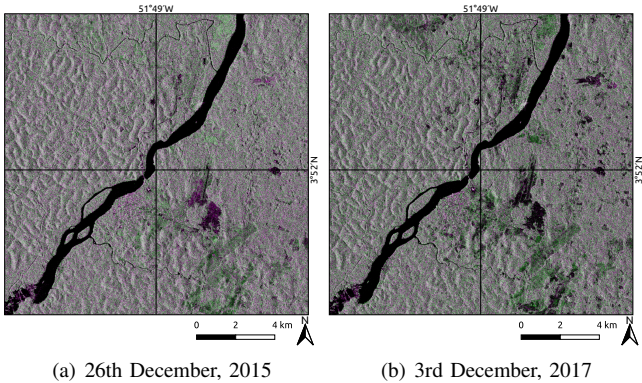


Fig. 5. Study area location. (preliminar)



**COMING
SOON!**

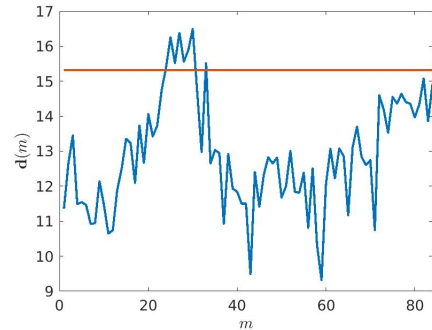
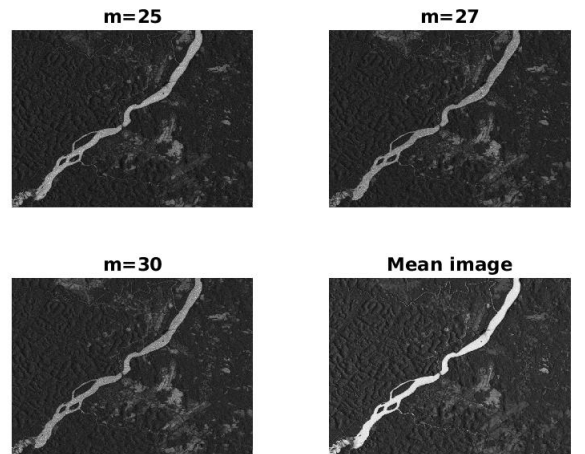
(c) Ground truth change/non-change samples

Fig. 6. Inserir caption...

is kept for further processing. Then, we are able to compute the squared mean differences vector \mathbf{d} and the matrix of absolute correlations \mathbf{R} .

The time change measures computed with \mathbf{d} are shown in Figure 7. The orange line in Figure 7a represents the median absolute deviation of \mathbf{d} , which allow us to notice times that differ expressively from the others. We can notice that times $m = 25, 27, 30$ are highlighted as having the most expressive changes. The images corresponding to these times can be seen in Figure 8.

The changes in space can be analyzed using the image obtained with \mathbf{R} , which is displayed in Figure 7c. Denoting the images' dimension as $N = 1538 \times 1556$, if we take the $[N / \log N]$ largest absolute correlations as those corresponding to possible change points, we obtain a matrix of zeros and

Fig. 7. Plot of $\mathbf{d}(m)$, $m = 1, \dots, 85$ with orange horizontal line indicating two times its median absolute deviation.Fig. 8. Images $\mathbf{X}^{(m)}$ from times m correspond to top-3 highest values of $\mathbf{d}(m)$ and the mean image $\bar{\mathbf{I}}$.

ones that is presented in Figure 7e. The white regions in Figure 7c (entries with value one) represent the change points, which seem to concentrate mainly on three regions: at the center, to the right of the river; at the top, on the left border of the river; and at the top left. Computing aggregated absolute differences to measure changes in space, we obtain Figure 7d. An image of detected changes corresponding to measures in Figure 7d can be obtained applying a thresholding method for grayscale images. Figure 7f shows the result of using Otsu's thresholding method [29] for aggregation of absolute differences.

The comparison of performance for the two change detection measures considered here can be checked in Figure 9, where a ROC curve is computed to check the correct detection of changes. WECS attains high true positive rates before the aggregation method, but both methods design competitive results. This performance differs from the ROC curve results in the previous section because the real images have a mean signal to noise ratio (SNR) of 3.9327, whereas the simulated images were generated with SNR of 0.2309. Hence, WECS is expected to have performance closer to the aggregation method in less noisy applications. The reference of correct change regions is shown in Figure 9a, which are determined using [XXXXX].

We can also compare the change detection methods using the F_1 -score accuracy measure. Denoting TP as the number of true positives (change pixels correctly detected), FP as the number of false positives (nonchange pixels flagged as change point) and FN as the total of false negatives (change points flagged as nonchange point), the F_1 -score is defined as

$$F_1 = 2 \frac{\text{Pr} \cdot \text{Re}}{\text{Pr} + \text{Re}},$$

where

$$\text{Pr} = \frac{\text{TP}}{\text{TP} + \text{FP}} \quad \text{and} \quad \text{Re} = \frac{\text{TP}}{\text{TP} + \text{FN}}.$$

Results of these three accuracy measures are presented in Table I. Results for aggregation of absolutes differences correspond to two types of thresholds: Otsu's method and Kittler-Illingworth [30]. We can observe that WECS presents the highest value of F_1 -score, which means it has a better performance than the competing method.

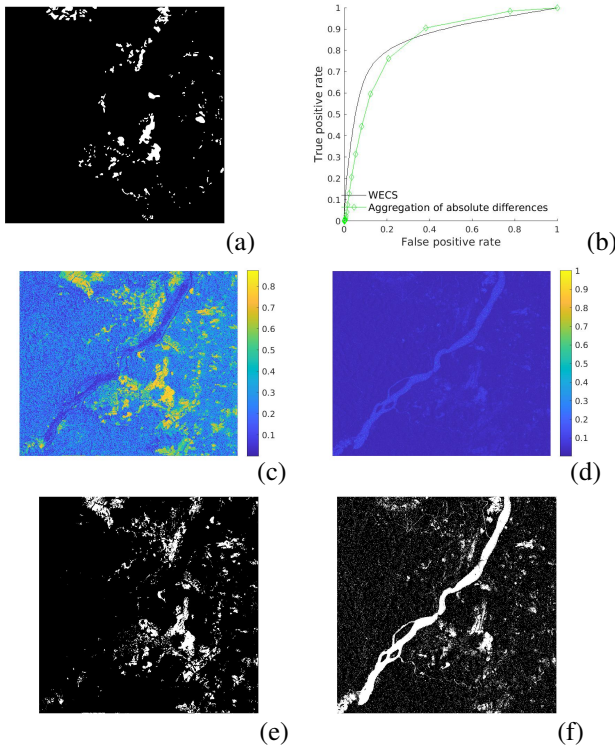


Fig. 9. Change points in space of the forest data. (a) Regions (in white) where changes should be detected. (b) ROC curve for detection of changing regions. (c) Matrix of absolute correlations obtained with WECS. (d) Change measures from aggregation of absolute differences. (e) Change regions detected by highlighting the $[N / \log N]$ largest correlations in \mathbf{R} (N denoting the image's dimension). (f) Change regions detected using aggregated absolute differences and Otsu's thresholding.

IV. DISCUSSION

We present a novel way of detecting changes in multi-temporal satellite images, WECS. The procedure is based on wavelet energies from both the estimated individual coefficients as well as the whole mean image. It makes use of correlation screening for ultra-high dimensional data. Thereupon, WECS is expected to provide a sample of points in space in a way that

TABLE I
ACCURACY MEASURES F_1 -SCORE, PRECISION (Pr) AND RECALL (Re)
COMPUTED FROM DETECTION OF CHANGING REGIONS IN THE FOREST DATA
USING WECS (TAKING THE $[N / \log N]$ LARGEST CORRELATIONS AS
CORRESPONDING TO CHANGE) AND THE AGGREGATION OF ABSOLUTE
DIFFERENCES WITH OTSU AND KITTLER-ILLINGWORTH'S (KI)
THRESHOLDS.

	Aggregated - Otsu	Aggregated - KI	WECS
F_1 -score	0.2231	0.2163	0.3253
Pr	0.1369	0.1296	0.2390
Re	0.6022	0.6526	0.5094

such set, contains real change points with high probability. The proposed method's performance is shown using both simulated and real data. The proposed method is useful to detect spatio-temporal change points, which is illustrated on data analyses. The method is employed to analyze a time series of 84 images of a forest.

REFERENCES

- [1] T. L. Barreto, R. A. Rosa, C. Wimmer, J. B. Nogueira, J. Almeida, and F. A. M. Cappabianco, "Deforestation change detection using high-resolution multi-temporal X-band SAR images and supervised learning classification," in *2016 IEEE International Geoscience and Remote Sensing Symposium (IGARSS)*. Beijing, China: IEEE, 2016, pp. 5201–5204.
- [2] Y. Ban and O. A. Yousif, "Multitemporal spaceborne SAR data for urban change detection in China," *IEEE Journal of Selected Topics in Applied Earth Observations and Remote Sensing*, vol. 5, no. 4, pp. 1087–1094, 2012.
- [3] C. Scher, N. C. Steiner, and K. C. McDonald, "Mapping seasonal glacier melt across the Hindu Kush Himalaya with time series synthetic aperture radar (SAR)," *The Cryosphere*, vol. 15, no. 9, pp. 4465–4482, 2021.
- [4] Y. Ban and O. Yousif, "Change detection techniques: A review," in *Multitemporal Remote Sensing*, Y. Ban, Ed. Cham: Springer, 2016, pp. 19–43.
- [5] L. Bruzzone and D. F. Prieto, "Automatic analysis of the difference image for unsupervised change detection," *IEEE Transactions on Geoscience and Remote Sensing*, vol. 38, no. 3, pp. 1171–1182, 2000.
- [6] T. Celik, "Change detection in satellite images using a genetic algorithm approach," *IEEE Geoscience and Remote Sensing Letters*, vol. 7, no. 2, pp. 386–390, 2010.
- [7] G. Quin, B. Pinel-Puyssegur, J.-M. Nicolas, and P. Loreaux, "MIMOSA: An automatic change detection method for SAR time series," *IEEE Transactions on Geoscience and Remote Sensing*, vol. 52, no. 9, pp. 5349–5363, 2014.
- [8] S. Saha, F. Bovolo, and L. Bruzzone, "Change detection in image time-series using unsupervised LSTM," *IEEE Geoscience and Remote Sensing Letters*, 2020.
- [9] F. Bovolo and L. Bruzzone, "The time variable in data fusion: A change detection perspective," *IEEE Geoscience and Remote Sensing Magazine*, vol. 3, no. 3, pp. 8–26, 2015.
- [10] S. Liu, D. Marinelli, L. Bruzzone, and F. Bovolo, "A review of change detection in multitemporal hyperspectral images: Current techniques, applications, and challenges," *IEEE Geoscience and Remote Sensing Magazine*, vol. 7, no. 2, pp. 140–158, 2019.
- [11] T. Matsunaga, A. Iwasaki, S. Tsuchida, K. Iwao, J. Tanii, O. Kashimura, R. Nakamura, H. Yamamoto, S. Kato, K. Obata, K. Moura, and T. Tachikawa, "Current status of hyperspectral imager suite (HISUI) onboard International Space Station (ISS)," in *2017 IEEE International Geoscience and Remote Sensing Symposium (IGARSS)*. Fort Worth, USA: IEEE, 2017, pp. 443–446.
- [12] M. Jia and L. Wang, "Novel class-relativity non-local means with principal component analysis for multitemporal SAR image change detection," *International Journal of Remote Sensing*, vol. 39, no. 4, pp. 1068–1091, 2018.
- [13] B. Hou, Q. Wei, Y. Zheng, and S. Wang, "Unsupervised change detection in SAR image based on Gauss-log ratio image fusion and compressed projection," *IEEE Journal of Selected Topics in Applied Earth Observations and Remote Sensing*, vol. 7, no. 8, pp. 3297–3317, 2014.

- [14] B. Du, L. Ru, C. Wu, and L. Zhang, "Unsupervised deep slow feature analysis for change detection in multi-temporal remote sensing images," *IEEE Transactions on Geoscience and Remote Sensing*, vol. 57, no. 12, pp. 9976–9992, 2019.
- [15] Y. Chen, Z. Ming, and M. Menenti, "Change detection algorithm for multi-temporal remote sensing images based on adaptive parameter estimation," *IEEE Access*, vol. 8, pp. 106 083–106 096, 2020.
- [16] F. Bovolo and L. Bruzzone, "A detail-preserving scale-driven approach to change detection in multitemporal SAR images," *IEEE Transactions on Geoscience and Remote Sensing*, vol. 43, no. 12, pp. 2963–2972, 2005.
- [17] B. Vidakovic, *Statistical Modeling by Wavelets*. New York: John Wiley & Sons, 1999.
- [18] P. A. Morettin, A. Pinheiro, and B. Vidakovic, *Wavelets in Functional Data Analysis*. Cham: Springer, 2017.
- [19] A. M. Atto, E. Trouvé, Y. Berthoumieu, and G. Mercier, "Multidate divergence matrices for the analysis of SAR image time series," *IEEE Transactions on Geoscience and Remote Sensing*, vol. 51, no. 4, pp. 1922–1938, 2012.
- [20] N. Bouhel, G. Ginolhac, E. Jolibois, and A. Atto, "Multivariate statistical modeling for multi-temporal SAR change detection using wavelet transforms," in *2015 8th International Workshop on the Analysis of Multitemporal Remote Sensing Images (Multi-Temp)*. Annecy, France: IEEE, 2015, pp. 1–4.
- [21] T. Celik, "Multiscale change detection in multitemporal satellite images," *IEEE Geoscience and Remote Sensing Letters*, vol. 6, no. 4, pp. 820–824, 2009.
- [22] S. Cui and M. Datcu, "Statistical wavelet subband modeling for multi-temporal SAR change detection," *IEEE Journal of Selected Topics in Applied Earth Observations and Remote Sensing*, vol. 5, no. 4, pp. 1095–1109, 2012.
- [23] J. Fan, R. Li, C.-H. Zhang, and H. Zou, *Statistical Foundations of Data Science*. Boca Raton: CRC Press, 2020.
- [24] J. Fan and J. Lv, "Sure independence screening for ultrahigh dimensional feature space," *Journal of the Royal Statistical Society: Series B*, vol. 70, no. 5, pp. 849–911, 2008.
- [25] R. R. Coifman and D. L. Donoho, "Translation-invariant de-noising," in *Wavelets and statistics*, A. Antoniadis and G. Oppenheim, Eds. New York: Springer, 1995, pp. 125–150.
- [26] A. M. Atto, E. Trouvé, J.-M. Nicolas, and T. T. Lê, "Wavelet operators and multiplicative observation models—application to SAR image time-series analysis," *IEEE Transactions on Geoscience and Remote Sensing*, vol. 54, no. 11, pp. 6606–6624, 2016.
- [27] I. M. Johnstone and D. M. Titterington, "Statistical challenges of high-dimensional data," *Philosophical Transactions of the Royal Society A*, vol. 367, pp. 4237–4253, 2009.
- [28] K. Zhang, W. Zuo, Y. Chen, D. Meng, and L. Zhang, "Beyond a Gaussian denoiser: Residual learning of deep CNN for image denoising," *IEEE transactions on image processing*, vol. 26, no. 7, pp. 3142–3155, 2017.
- [29] N. Otsu, "A threshold selection method from gray-level histograms," *IEEE Transactions on Systems, Man, and Cybernetics*, vol. 9, no. 1, pp. 62–66, 1979.
- [30] J. Kittler and J. Illingworth, "Minimum error thresholding," *Pattern Recognition*, vol. 19, no. 1, pp. 41–47, 1986.